Far-field polarization-based sensitivity to sub-resolution displacements of a sub-resolution scatterer in tightly focused fields

Oscar G. Rodríguez-Herrera,[1]* David Lara,[2] and Chris Dainty[1]

[1]*Applied Optics, School of Physics, National University of Ireland, Galway, University Road, Galway, Ireland*
[2]*The Blackett Laboratory, Imperial College London, SW7 2BW, London, United Kingdom*
oscar.rodriguez@nuigalway.ie

Abstract: We present a system built to perform measurements of scattering-angle-resolved polarization state distributions across the exit pupil of a high numerical aperture collector lens. These distributions contain information about the three-dimensional electromagnetic field that results from the interaction of a tightly focused field and a sub-resolution scatterer. Experimental evidence proving that the system allows for high polarization-dependent sensitivity to sub-resolution displacements of a sub-resolution scatterer is provided together with the corresponding numerical results.

OCIS codes: (290.5820) Scattering measurements; (260.5430) Polarization; (120.5410) Polarimetry.

References and notes

1. E. Wolf, "Electromagnetic diffraction in optical systems. I. An integral representation of the image field," Proc. R. Soc. Lond. A Math. Phys. Sci. **253**(1274), 349–357 (1959).
2. B. Richards, and E. Wolf, "Electromagnetic diffraction in optical systems. II. Structure of the image field in an aplanatic system," Proc. R. Soc. Lond. A Math. Phys. Sci. **253**(1274), 358–379 (1959).
3. E. Wolf, and Y. Li, "Conditions for the validity of the Debye integral representation of focused fields," Opt. Commun. **39**(4), 205–210 (1981).
4. M. Mansuripur, "Distribution of light at and near the focus of high-numerical-aperture objectives," J. Opt. Soc. Am. A **3**(12), 2086–2093 (1986).
5. R. Kant, "An analytical solution of vector diffraction for focusing optical systems with Seidel aberrations I. Spherical aberration, curvature of field, and distortion," J. Mod. Opt. **40**(11), 2293–2310 (1993).
6. D. P. Biss, and T. G. Brown, "Primary aberrations in focused radially polarized vortex beams," Opt. Express **12**(3), 384–393 (2004).
7. P. Török, P. Varga, and G. Németh, "Analytical solution of the diffraction integrals and interpretation of wavefront distortion when light is focused through a planar interface between materials of mismatched refractive indices," J. Opt. Soc. Am. A **12**(12), 2660–2671 (1995).
8. H. Ling, and S. W. Lee, "Focusing of electromagnetic waves through a dielectric interface," J. Opt. Soc. Am. A **1**(9), 965–973 (1984).
9. P. Török, P. Varga, Z. Laczik, and G. R. Booker, "Electromagnetic diffraction of light focused through a planar interface between materials of mismatched refractive indices: an integral representation," J. Opt. Soc. Am. A **12**(2), 325–332 (1995).
10. V. Delaubert, N. Treps, G. Bo, and C. Fabre, "Optical storage of high-density information beyond the diffraction limit: A quantum study," Phys. Rev. A **73**(1), 013820 (2006).
11. J. M. Brok, and H. P. Urbach, "Simulation of polarization effects in diffraction problems of optical recording," J. Mod. Opt. **49**(11), 1811–1829 (2002).
12. P. Török, and M. Gu, "High-numerical-aperture optical microscopy and modern applications: introduction to the feature issue," Appl. Opt. **39**(34), 6277–6278 (2000).
13. P. Török, and P. R. T. Munro, "The use of Gauss-Laguerre vector beams in STED microscopy," Opt. Express **12**(15), 3605–3617 (2004).
14. Q. Zhan, and J. R. Leger, "Measurement of surface features beyond the diffraction limit with an imaging ellipsometer," Opt. Lett. **27**(10), 821–823 (2002).
15. A. Rohrbach, and E. H. K. Stelzer, "Optical trapping of dielectric particles in arbitrary fields," J. Opt. Soc. Am. A **18**(4), 839–853 (2001).
16. K.-H. Shuster, "Radial polarization - rotating optical arrangement and microlithographic projection exposure system incorporating said arrangement", US Patent 6191880B1 (2001).
17. D. McGloin, "Optical tweezers: 20years on," Philos. Trans. R. Soc. Lond. A **364**(1849), 3521–3537 (2006).

#124017 - $15.00 USD Received 9 Feb 2010; revised 27 Feb 2010; accepted 28 Feb 2010; published 3 Mar 2010

18. R. L. Eriksen, V. R. Daria, and J. Gluckstad, "Fully dynamic multiple-beam optical tweezers," Opt. Express **10**(14), 597–602 (2002).
19. F. Kulzer, and M. Orrit, "Single-molecule optics," Annu. Rev. Phys. Chem. **55**(1), 585–611 (2004).
20. W. Chen, and Q. Zhan, "Three-dimensional focus shaping with cylindrical vector beams," Opt. Commun. **265**(2), 411–417 (2006).
21. J. T. Fourkas, "Rapid determination of the three-dimensional orientation of single molecules," Opt. Lett. **26**(4), 211–213 (2001).
22. A. De Martino, S. Ben Hatit, and M. Foldyna, "Mueller polarimetry in the back focal plane," Proc. SPIE **6518**, 65180X (2007).
23. S. Ben Hatit, M. Foldyna, A. De Martino, and B. Drévillon, "Angle-resolved Mueller polarimeter using a microscope objective," Phys. Status Solidi., A Appl. Mater. Sci. **205**(4), 743–747 (2008).
24. In the figure, the dashed lines box represents a part of the experimental setup that is orthogonal to the plane of the optical bench.
25. F. Delplancke, "Automated high-speed Mueller matrix scatterometer," Appl. Opt. **36**(22), 5388–5395 (1997).
26. D. Lara, and C. Dainty, "Axially resolved complete mueller matrix confocal microscopy," Appl. Opt. **45**(9), 1917–1930 (2006).
27. W. S. Bickel, and W. M. Bailey, "Stokes vectors, Mueller matrices and polarized scattered light," Am. J. Phys. **53**(5), 468–478 (1985).
28. E. Compain, S. Poirier, and B. Drévillon, "General and self-consistent method for the calibration of polarization modulators, polarimeters, and mueller-matrix ellipsometers," Appl. Opt. **38**(16), 3490–3502 (1999).
29. A. De Martino, Y.-K. Kim, E. Garcia-Caurel, B. Laude, and B. Drévillon, "Optimized Mueller polarimeter with liquid crystals," Opt. Lett. **28**(8), 616–618 (2003).
30. To speed-up the calibration of the system, and reduce the noise in the measurements, we applied a 4 × 4 binning to the original 1024 × 768 pixel images. This reduced the time spent in the calibration from ~6 hours to ~30 minutes and increased the pixel alignment accuracy. The same binning was applied to all our experimental data.
31. The Mueller matrices presented in this section were obtained from the average of 25 measurements, for each combination polarizer-analyzer, to minimize the effect of statistical errors.
32. J. D. Jackson, *Classical Electrodynamics* (John Wiley & Sons, 1999).
33. K. Lindfors, A. Priimagi, T. Setälä, A. Shevchenko, A. T. Friberg, and M. Kaivola, "Local polarization of tightly focused unpolarized light," Nat. Photonics **1**(4), 228–231 (2007).
34. This approximation is commonly used in the analysis of the image formation of a point-scatterer.
35. C. J. R. Sheppard, and T. Wilson, "The Image of a Single Point in Microscopes of Large Numerical Aperture," Proc. R. Soc. Lond. A Math. Phys. Sci. **379**(1776), 145–158 (1982).
36. The results for the gold nano-sphere were obtained as the average of 5 measurements for each combination polarizer-analyzer to minimize the effect of statistical errors.

1. Introduction

When a beam of light is brought to a focus by an optical system with sufficiently high numerical aperture (NA), the electromagnetic (EM) focused field may possess a significant component parallel to the direction of propagation of the original beam (e.g. along the z-axis), in addition to the two components orthogonal to this direction (e.g. x and y). In other words, at every position inside the focal region the EM field can have components oscillating in three mutually perpendicular directions. This property of focused fields became well known since the publication of the vectorial theory of diffraction [1,2], where Richards and Wolf analyzed the field focused by an aplanatic system. Subsequent work by other authors proved that this is true as long as the NA is sufficiently large [3,4], even if the system is not aplanatic, for example in the presence of optical aberrations [5–7], or when the light is focused through a dielectric interface [7–9]. The vectorial structure of the EM field in the focal region of a lens, as predicted by the vectorial theory of diffraction [1,2], also depends on the polarization state of the incident light. This property becomes important as the NA is increased, and has been studied for several years now. Its most common intended applications reside in the areas of optical storage [10,11], microscopy and scanning optical microscopy [12–14], photonic force microscopy [15], lithography [16], laser micro-fabrication, particle guiding or trapping [17,18], and single molecule imaging [10,19–21].

When a small sample interacts with a tightly focused field, the EM field that results is also a three-dimensional vectorial field. Clearly, the sample will affect all three components of the focused field. For example, in the case of a single molecule the resulting EM field will depend on the orientation of the molecule's electric dipole moment, and in the case of a data storage medium, sub-diffraction-limit features of the recorded medium will also interact with any or all of the three vectorial components of the illumination. The characterization of three-

#124017 - $15.00 USD Received 9 Feb 2010; revised 27 Feb 2010; accepted 28 Feb 2010; published 3 Mar 2010

dimensional scattered fields is important in the analysis of light-matter interaction in the focal region of high-NA imaging systems.

In this paper, we present a system built to measure the scattering-angle-resolved polarization state distribution of the three-dimensional field scattered by a sub-resolution specimen in the focal region of a high-NA lens. A similar kind of analysis has been reported in the past that uses incoherent illumination to estimate the critical dimensions of diffraction gratings [22,23]. Our approach makes use of coherent laser illumination, which, at the focus, produces a coherent superposition of all contributions from different positions of the pupil of the focusing system. Hence, the distributions measured with the system presented herein are related to the three-dimensional field scattered by the sub-resolution object via a three-dimensional to two-dimensional transformation. Figure 1 is a schematic diagram of the working principle of our system. Incident beam-like field, $\mathbf{E}^{(0)}$, is focused by a high-NA focusing lens originating a non-negligible longitudinal component in its focal region, $E_z^{(1)}$, in addition to the two transversal components, $E_x^{(1)}$ and $E_y^{(1)}$. For clarity this latter component is not shown in the diagram. After the interaction of the focused field with a sub-resolution specimen in the focal region, a three-dimensional scattered field, $\mathbf{E}^{(s)}$, is produced. The scattered field then propagates to a high-NA collector lens that collimates it, creating a beam-like field, $\mathbf{E}^{(2)}$, with negligible longitudinal component. The longitudinal component of the scattered field, $E_z^{(s)}$, is combined with the transversal components by the collector lens depending on the scattering angle. Therefore, by analyzing the scattering-angle-resolved polarization state distribution across the exit pupil of the collector lens, it is possible to reconstruct, up to an arbitrary phase, the scattered field distribution just before the collector lens, which carries polarization information that originates from the three dimensional nature of the focused field.

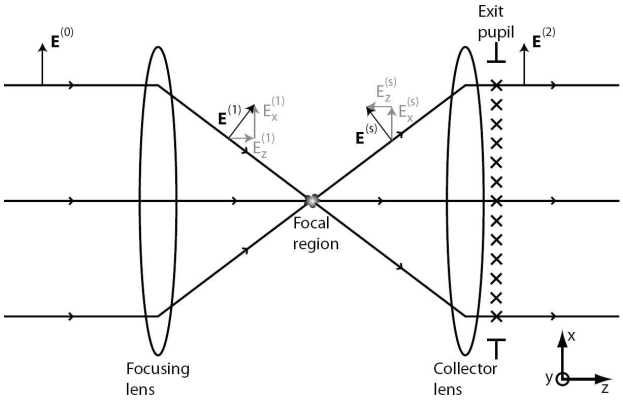

Fig. 1. Schematic diagram of the working principle of our system. The longitudinal component of the scattered field, $E_z^{(s)}$, is combined with the transversal components by the collector lens. The crosses indicate sample points in the exit pupil where the polarization state is analyzed.

In the following sections, we present numerical and experimental results showing that, when the complete three-dimensional nature of the focused field is considered, high sensitivity to sub-resolution displacements of a sub-resolution specimen is achieved by measuring the scattering-angle-resolved polarization state distribution across the exit pupil of the high-NA collector lens. The paper is organized as follows: in section 2 we present the experimental setup and the generation of the incident polarization states. In section 3 we discuss the calibration of the system. In section 4 we describe briefly the numerical analysis done to assess the performance of our system. In section 5 we present numerical and experimental results for sub-resolution displacements of a point-scatterer. Finally, in section 6, we present our conclusions and remarks on the future of this research.

#124017 - $15.00 USD Received 9 Feb 2010; revised 27 Feb 2010; accepted 28 Feb 2010; published 3 Mar 2010

2. Experimental setup

The system built in this work is a spatially resolved Mueller matrix polarimeter with two Pockels cells as polarization state generator (PSG) and four CCD cameras as simultaneous division-of-amplitude polarization state analyzer (PSA). We refer to it as the vectorial polarimeter. Figure 2 is a schematic diagram of the system. The total irradiance of the light coming from laser LS (MellesGriot 85-GCA-005, $\lambda = 532$nm), is controlled using two neutral density filters, NDF and NDFW, before a Glan-Taylor vertical polarizer (MellesGriot 03PTA401), P1. Mirror M1 was introduced to bend the light path towards the longest side of the optical bench. The light transmitted by P1 is then sent to a pair of Pockels cells (Linos LM0202), PC1 and PC2, which can produce any homogeneous incident polarization state over the Poincaré sphere (section 2.1). Then, the light beam is sent to a spatial filter, formed by objective OBJ1 (Linos 038722) and pinhole PH, where it is also expanded and later collimated by lens L1. Aperture stop IRIS3, with a diameter of ~7mm, blocks the rim of the beam to produce an incident beam with a gaussian profile flatter than the original laser beam. The light beam is then reflected by beam-splitter BS1 towards mirror M2, at 45° from the horizontal, where the light path is bent downwards towards the high-NA objective, OBJ2, which focuses the light onto the specimen SMP. After the interaction of the three-dimensional focused field with the specimen, the three-dimensional scattered field propagates to the collector lens where it is transformed in a beam-like scattering-angle-resolved distribution. Since the system was built to work in the reflection configuration, the high-NA objective, OBJ2, acts as the collector lens as well. Finally, the exit pupil of the collector lens is imaged onto the position of the four simultaneous linearly independent polarization detectors, CCD1-CCD4 (Point Grey Research, Inc. Flea2-08S2M-C). The four images of the ~7mm pupil are produced by the relay optical system formed by lenses L2-L5 and mirrors M3-M4. The magnification of this last optical relay is 0.57. Mirror M5 and apertures IRIS1-IRIS2 and IRIS4 are used as aids in the alignment of the system. IRIS4 is also used to block back-reflections and prevent them from reaching the CCD cameras. The shaded part of Fig. 2 represents an auxiliary system used to position the sub-resolution specimen in the focal region of the high-NA objective [24]. This part of the system is explained in section 4.

The division-of-amplitude PSA formed by non-polarizing beam-splitters BS2-BS3, polarizing beam-splitter PBS, quarter-wave-plate QWP, and linear polarizers P2-P3, measures the linear vertically and horizontally polarized components of the scattered light, CCD1 and CCD2, respectively, the component linearly polarized at + 45°, CCD3, and the left-circular component, CCD4. This configuration was chosen to obtain simultaneous measurements of the spatially resolved Stokes vectors with the four CCD cameras, and it has been used in the past, albeit with point detectors, with excellent results [25,26].

2.1 Modulation of the Pockels cells

To generate the incident polarization states of the beam to be focused, we modulated the voltage sent to the Pockels cells via a digital-to-analog board (IOtech DaqBoard/2000). Since the Pockels cells do not exhibit diattenuation, and they are non-depolarizing, they can be considered as linear retarders with retardance proportional to the voltage applied. PC1 and PC2 were oriented such that their fast axis was at −45° and 0°, respectively, from the horizontal. Six different incident polarization states were used in the measurements presented here. The pairs of retardances introduced generated the following polarization states: linear horizontal (H), linear vertical (V), linear at + 45° (+), linear at −45° (-), right-circular (R), and left-circular (L). Table 1 shows the actual values, in wavelengths, of the six retardance pairs introduced with the Pockels cells and the corresponding incident polarization states used in the measurements with our system; Δ_1 and Δ_2 are the retardance introduced in PC1 and PC2, respectively.

#124017 - $15.00 USD Received 9 Feb 2010; revised 27 Feb 2010; accepted 28 Feb 2010; published 3 Mar 2010

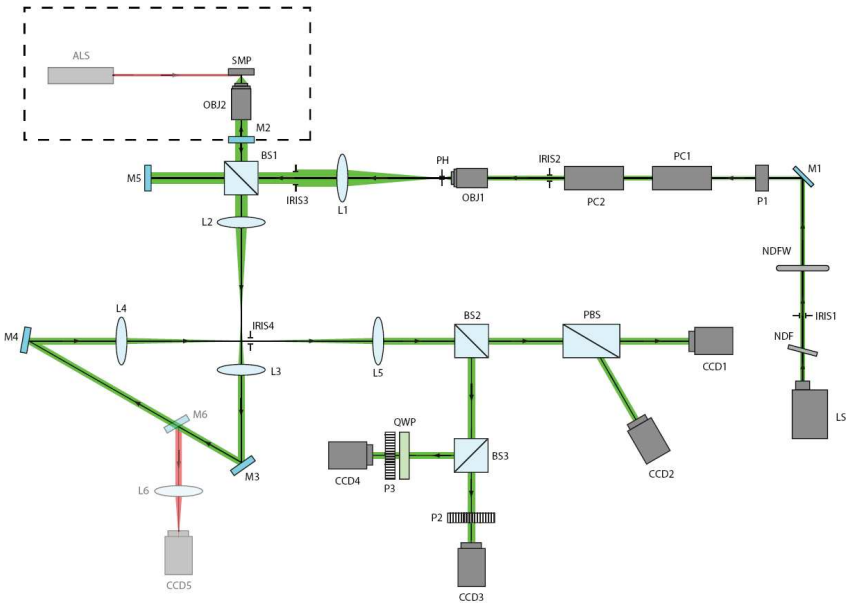

Fig. 2. Diagram of the vectorial polarimeter. The light path in green is the path followed by the light that forms the image of the exit pupil in cameras CCD1-CCD4. The shaded part of the system, which corresponds to the red light path, is the path followed by the light used to produce the auxiliary image discussed in section 5. CCD2 is at 45° from the direction of the beam incident on the polarizing beam-splitter, PBS, because the beam-splitter is designed to give this angular separation between the vertical and horizontal polarization components.

Table 1. Pairs of retardance introduced in the Pockels cells in wavelength units.

Polarization state	Δ_1	Δ_2
+	$-\frac{3}{4}$	$-\frac{3}{4}$
H	$-\frac{1}{2}$	$-\frac{5}{8}$
R	$-\frac{1}{4}$	$-\frac{1}{2}$
V	0	$-\frac{3}{8}$
-	$-\frac{3}{4}$	$-\frac{1}{4}$
L	$-\frac{1}{4}$	0

2.2 Detection of the spatially resolved Stokes parameters

The experimental data obtained with the vectorial polarimeter can be used to calculate the back focal plane Mueller matrix of the specimen using the simple arithmetic relations between the measured irradiances and the elements of the matrix involved for each combination polarizer-analyzer [27]. For each of the six polarization states generated by the PSG, the full Stokes vector was measured at every pixel in the image of the pupil/back-focal-plane of the collector lens. The actual expressions used to calculate the Mueller matrix

#124017 - $15.00 USD Received 9 Feb 2010; revised 27 Feb 2010; accepted 28 Feb 2010; published 3 Mar 2010

elements are shown in Fig. 3. As the figure indicates, the elements of the Mueller matrix are obtained as the combination of different irradiance measurements – on different cameras and for different incident polarization states. These expressions are applied at every pixel on the pupil of the collector lens after subtracting the corresponding background dark image. Thus, the alignment of the CCD cameras, pixel by pixel, is paramount in the correct calculation of the Mueller matrix distribution.

The CCD cameras were aligned before including the objective in the system, using the image of a circular aperture at the position where the objective's pupil is located when the system is completely mounted. The aperture was illuminated by an extended incoherent light source pointing from the position of the specimen towards the relay optical system that images the exit pupil of the collector lens. The alignment was made using the cross-correlation between the image of the circular aperture on one camera (set as the reference), and the corresponding images on the rest of the cameras. The position of the peak of the cross-correlation showed how accurately the images on the cameras overlapped. The correct azimuthal orientation of the cameras was also verified using a cross-correlation method. A circular aperture with a thin vertical wire along its diameter was used to identify rotation errors. The precision of the alignment was calculated to be ± 1/2 of a CCD pixel (4.65 microns), however, the experimental images were pixel-binned with a 4 × 4 kernel. The effective precision of the correspondence of the data pixels was therefore ± 1/8 of a data pixel.

3. System calibration

Robust calibration of the experimental setup is critical in our measurements. Because of the influence of Fresnel parameters in the polarization, and spurious inhomogeneities of the polarization components, every single optical element in an experimental setup may introduce polarization artifacts. This limits the accuracy with which the Mueller matrix can be measured, and needs to be addressed carefully.

m_{11} ✳ ✳	m_{12} ↔ ✳	m_{13} ⤢ ✳	m_{14} ↻ ✳
$\frac{1}{2}[(I_{HH}+I_{HV})+(I_{VH}+I_{VV})]$	$\frac{1}{2}[(I_{HH}+I_{HV})-(I_{VH}+I_{VV})]$	$\frac{1}{2}[(I_{+H}+I_{+V})-(I_{-H}+I_{-V})]$	$\frac{1}{2}[(I_{RH}+I_{RV})-(I_{LH}+I_{LV})]$
m_{21} ✳ ↔	m_{22} ↔ ↔	m_{23} ⤢ ↔	m_{24} ↻ ↔
$\frac{1}{2}[(I_{HH}+I_{VH})-(I_{HV}+I_{VV})]$	$\frac{1}{2}[(I_{HH}-I_{VH})-(I_{HV}-I_{VV})]$	$\frac{1}{2}[(I_{+H}-I_{+V})-(I_{-H}-I_{-V})]$	$\frac{1}{2}[(I_{RH}-I_{RV})-(I_{LH}-I_{LV})]$
m_{31} ✳ ⤢	m_{32} ↔ ⤢	m_{33} ⤢ ⤢	m_{34} ↻ ⤢
$2[I_{H+}+I_{V+}]-m_{11}$	$2[I_{H+}-I_{V+}]-m_{12}$	$2[I_{++}-I_{-+}]-m_{13}$	$2[I_{R+}-I_{L+}]-m_{14}$
m_{41} ✳ ↺	m_{42} ↔ ↺	m_{43} ⤢ ↺	m_{44} ↻ ↺
$-2[I_{HL}+I_{VL}]+m_{11}$	$-2[I_{HL}-I_{VL}]+m_{12}$	$-2[I_{+L}-I_{-L}]+m_{13}$	$-2[I_{RL}-I_{LL}]+m_{14}$

Note: ✳ Unpolarized ⤢ Linear at 45°
↔ Linear horizontal ↻ Lefft-circular

Fig. 3. Measurements and operations necessary to obtain the 16 elements of the Mueller matrix for every data pixel in our system. From left to right, the first symbol, and subscript of I, represents the polarization state of the incident light whereas the second symbol, and subscript, represents the analyzer used in the corresponding measurement. The convention followed for the subscripts is the same as in section 2.1. The unpolarized component, for the incident light, and the total irradiance, for the analyzer, were obtained as the incoherent superposition of the H and V components accordingly.

The method used to calibrate our system is an extension of the eigenvalue calibration method (ECM) to be used in double-pass (ECM-DP) [28,26]. The calibration samples used are the four optimum calibration samples given by De Martino *et al.* [29], namely: a linear polarizer at two different orientations (0° and 90°, with respect to the horizontal, $\mathbf{B_1}$ and $\mathbf{B_2}$, respectively), a wave-plate with retardance of λ/4 in double-pass (oriented at ~30°, with respect to the horizontal, $\mathbf{B_3}$), and free space ($\mathbf{B_0}$). The calibration method was implemented

#124017 - $15.00 USD Received 9 Feb 2010; revised 27 Feb 2010; accepted 28 Feb 2010; published 3 Mar 2010

pixel by pixel across the aperture of the incident beam to calibrate the whole area of interest [30]. Since the calibration of our system with the ECM-DP requires the measurement of the Mueller matrix of the four calibration samples, it is impractical to do the calibration with the high-NA objective in place. This is due to the typically short focal length, and even shorter working distance, of high-NA microscope objectives. Thus, the objective was removed during this part of the calibration. A flat auxiliary mirror was placed, just after the calibration samples, normal to the incident light path. After the first-pass through the calibration sample, the light was reflected back to the optical system passing a second time through the calibration sample. This double-pass configuration introduces an ambiguity in the definition of the polarization orientation, and handedness, due to the change in the direction of propagation. However, as discussed in [26], once a reference orientation has been chosen, whether it corresponds to the first-pass or the second-pass, the effect of the reflection can be included in the system calibration matrices.

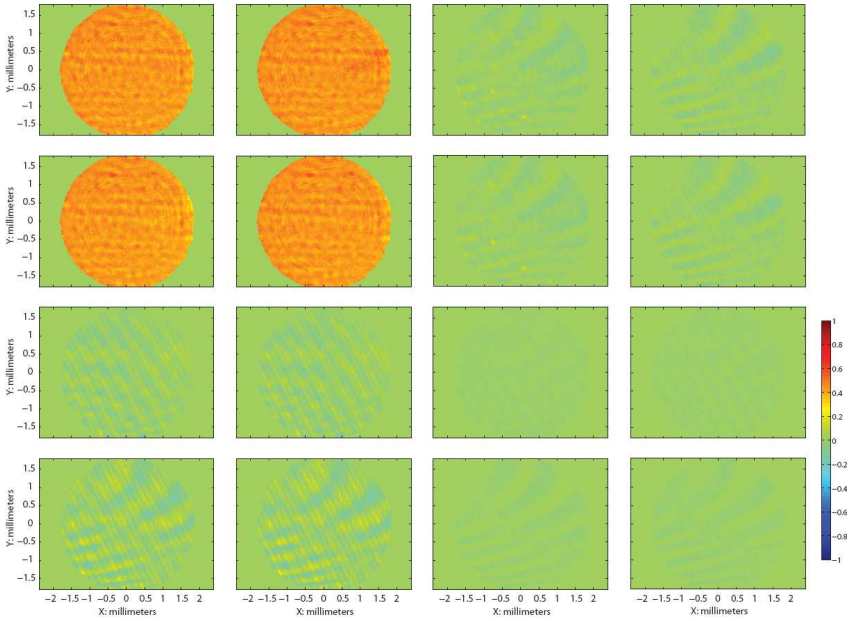

Fig. 4. Calibrated Mueller matrix of the horizontal polarizer, within the aperture of the incident beam, as obtained with our system.

As an example of the accuracy of the system, Fig. 4 shows the calibrated Mueller matrix for a linear horizontal polarizer [31]. Despite some residual artifacts present in the elements of the Mueller matrix as interference fringes, the calibrated Mueller matrix of the horizontal polarizer is in agreement with its theoretical counterpart. Table 2 contains the mean and standard deviation of each coefficient of the Mueller matrix distribution in Fig. 4 next to its corresponding theoretical matrix. The table shows this comparison for the four samples used in the calibration. The experimental measurements used for Table 2 were not part of the calibration routine, they were independent measurements made after calibration. The exact values of the transmittance (τ), angle of orientation (θ), retardance (Δ), and diattenuation (Ψ) of the corresponding theoretical matrices were not known. They were fitted with the average parameters obtained during the ECM [26,28,29]. The difference between both matrices, for each calibration sample, was found to be below one standard deviation. As error metric, we subtracted the mean experimental matrices from the theoretical ones, and calculated the RMS of the 16 coefficient differences for each sample. This number is also shown in Table 2.

#124017 - $15.00 USD Received 9 Feb 2010; revised 27 Feb 2010; accepted 28 Feb 2010; published 3 Mar 2010

Table 2. Fitted theoretical Mueller matrix and mean and standard deviation of the pixel value distribution, within the aperture of the beam, for the Mueller matrix of each calibration sample. Δ and Ψ are the ellipsometric angles in radians.

Sample	Mean	Standard deviation	Fitted theoretical	RMS error
B_0 $\tau = 1$	$\begin{pmatrix} 1.01 & 0.00 & 0.00 & 0.01 \\ 0.00 & 1.00 & -0.03 & -0.03 \\ -0.02 & 0.07 & 0.98 & 0.00 \\ -0.03 & 0.04 & -0.04 & 1.02 \end{pmatrix}$	$\begin{pmatrix} 0.03 & 0.03 & 0.02 & 0.03 \\ 0.03 & 0.03 & 0.01 & 0.01 \\ 0.02 & 0.01 & 0.03 & 0.02 \\ 0.04 & 0.02 & 0.02 & 0.03 \end{pmatrix}$	$\begin{pmatrix} 1 & 0 & 0 & 0 \\ 0 & 1 & 0 & 0 \\ 0 & 0 & 1 & 0 \\ 0 & 0 & 0 & 1 \end{pmatrix}$	**0.03**
B_1 $\tau = 0.86$ $\theta = 0.0002°$	$\begin{pmatrix} 0.44 & 0.44 & 0.00 & 0.00 \\ 0.43 & 0.44 & 0.00 & 0.00 \\ 0.00 & 0.00 & 0.00 & 0.00 \\ 0.00 & 0.00 & 0.00 & 0.00 \end{pmatrix}$	$\begin{pmatrix} 0.03 & 0.03 & 0.03 & 0.04 \\ 0.03 & 0.03 & 0.03 & 0.03 \\ 0.04 & 0.04 & 0.01 & 0.01 \\ 0.06 & 0.06 & 0.02 & 0.02 \end{pmatrix}$	$\begin{pmatrix} 0.43 & 0.43 & 0.00 & 0.00 \\ 0.43 & 0.43 & 0.00 & 0.00 \\ 0.00 & 0.00 & 0.00 & 0.00 \\ 0.00 & 0.00 & 0.00 & 0.00 \end{pmatrix}$	**0.03**
B_2 $\tau = 0.085$ $\theta = 90.86°$	$\begin{pmatrix} 0.43 & -0.43 & 0.00 & 0.01 \\ -0.42 & 0.42 & 0.00 & -0.01 \\ -0.01 & 0.01 & 0.00 & 0.00 \\ -0.02 & 0.02 & 0.00 & 0.00 \end{pmatrix}$	$\begin{pmatrix} 0.05 & 0.05 & 0.06 & 0.03 \\ 0.05 & 0.05 & 0.05 & 0.03 \\ 0.03 & 0.05 & 0.01 & 0.01 \\ 0.05 & 0.05 & 0.02 & 0.01 \end{pmatrix}$	$\begin{pmatrix} 0.43 & -0.43 & -0.01 & 0.00 \\ -0.43 & 0.43 & 0.01 & 0.00 \\ -0.01 & 0.01 & 0.00 & 0.00 \\ 0.00 & 0.00 & 0.00 & 0.00 \end{pmatrix}$	**0.01**
B_3 $\tau = 1$ $\theta = 29.66°$ $\Delta = -1.5236$ $\Psi = 0.7652$	$\begin{pmatrix} 1.03 & -0.01 & -0.01 & -0.01 \\ 0.02 & 0.30 & 0.43 & 0.89 \\ 0.00 & 0.46 & 0.76 & -0.49 \\ 0.03 & -0.85 & 0.59 & 0.01 \end{pmatrix}$	$\begin{pmatrix} 0.09 & 0.03 & 0.04 & 0.03 \\ 0.05 & 0.08 & 0.05 & 0.07 \\ 0.08 & 0.06 & 0.06 & 0.08 \\ 0.05 & 0.07 & 0.09 & 0.06 \end{pmatrix}$	$\begin{pmatrix} 1.00 & 0.00 & 0.00 & 0.00 \\ 0.00 & 0.30 & 0.42 & 0.86 \\ 0.00 & 0.42 & 0.75 & -0.51 \\ 0.00 & -0.86 & 0.51 & 0.05 \end{pmatrix}$	**0.03**

Two sets of interference fringes can be observed in Fig. 4, the calibrated Mueller matrix of the horizontal polarizer. The alignment of the cameras was verified to exclude orientation artifacts as the origin of the fringes. The low frequency fringes originate in unavoidable back-reflections in the pane that covers the CCD detector in the cameras. The effect of these back-reflections can be reduced, for instance, using a CCD with no pane. In this case, the CCD detector would be exposed to the environment and it might get dusty easily. Another alternative is to change the PSA into a sequential Stokes polarimeter with a single CCD, but the measurement of the Stokes vector would not be simultaneous as in a division-of-amplitude polarimeter. The dichroic linear polarizer at + 45° in front of CCD3 is responsible for the high frequency fringes. To get rid of them, the dichroic polarizer may be substituted by a better quality crystal polarizer such as a Glan-Taylor.

The objective used in the measurements with our system (Olympus UPLSAPO 100x oil immersion, NA = 1.4 in n = 1.518 immersion oil) was removed during the calibration with the ECM-DP. However, it is important to quantify the polarization artifacts that might be introduced by the objective. A 0.99 NA concave spherical reference surface (custom made by IC Optical Systems Ltd.) was used to assess the effect of the objective on the polarization. The sphere was made of BK7 glass and had a surface quality of λ/2 over the whole NA. We measure the Mueller matrix of the reference sphere in the following way: when the center of curvature of the reference surface coincides with the focus of the objective, each ray exiting the objective impinges normally upon the surface of the reference sphere, and is reflected in the same direction of the incident ray. The ray is only partially reflected because the reference sphere lacks of any high reflectivity coating. Since the reflection on the sphere is normal for each ray, it introduces the same phase shift for all rays. Therefore, any inhomogeneous variation in the polarization state of the reflected light, measured across the exit pupil of the

#124017 - $15.00 USD Received 9 Feb 2010; revised 27 Feb 2010; accepted 28 Feb 2010; published 3 Mar 2010

objective, would be introduced by the objective itself. Since it was impractical to fill the reference sphere with immersion oil for the characterization of the objective, a high-NA dry objective (Olympus MPLAPO 100x, NA = 0.95 in air) was used in this part of the calibration. According to the manufacturer both objectives have similar polarization properties, they were made with the same quality standards, and thus, the same order of polarization artifacts measured for the dry objective was assumed for the oil immersion objective. This assumption appears to be appropriate according to our experimental results; this point is further discussed in section 5. Figure 5 is the Mueller matrix of the spherical reference surface as measured with our system using the MPLAPO dry objective. The matrix matches the Mueller matrix of free space within one standard deviation. The reduced transmittance is due to the low reflectance of the uncoated reference sphere. This indicates that, in double-pass, the polarization artifacts introduced by the objective are, at least at a first approximation, negligible. Note that the Mueller matrix of the spherical reference surface corresponds to free space instead of a mirror because we chose the first-pass coordinate system to represent our double-pass measurements [26].

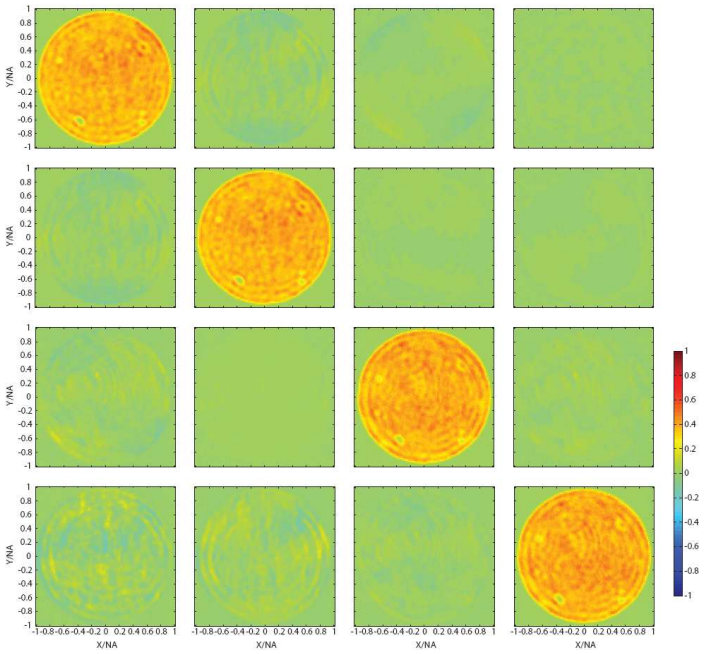

Fig. 5. Mueller matrix of the reference sphere used to characterize the polarization artifacts introduced by the high-NA microscope objective. The spot in the lower-left corner of the pupil is due to a scratch in the surface of the sphere produced accidentally during the alignment. Note that the images correspond to a zoom-in on the region of interest, i.e. the exit pupil.

4. Numerical analysis

For the sake of comparison with our experimental results, and to assess the reliability of the measurements, we modeled the performance of our system using analytical and numerical methods readily available, an applied them to a point-scatterer as specimen. This case, of course, has no experimental counterpart. However, if the scatterer is much smaller than the wavelength (λ = 532nm in this case), it is appropriate to consider it as a point-scatterer [32]. The specimen used in the measurements presented herein is an 80nm diameter gold nano-sphere. This kind of specimen has been modeled before as a point-scatterer, at visible frequencies, with good results [33].

First, the field distribution in the focal region was calculated from direct integration of Debye-Wolf integrals [1,2]. Then, the scattered field was calculated using the analytical

#124017 - $15.00 USD Received 9 Feb 2010; revised 27 Feb 2010; accepted 28 Feb 2010; published 3 Mar 2010

solution for the field radiated by an electric dipole [34], with dipole moment proportional to the incident EM field. Finally, the effect of the collector lens was modeled with the geometrical transformation given by Sheppard and Wilson [35]. Alternatively, the so-called generalized Jones matrices, introduced by Török *et al.* [9], may be used to model the effect of the collector lens – both are analytically equivalent. The $E_x^{(2)}$ and $E_y^{(2)}$ field components obtained this way were then used to calculate the Stokes parameters distribution across the exit pupil of the collector lens, which are the results reported in the following section, using the definitions given in Eq. (1), where E_k^* is the complex conjugate of E_k for k = x,y.

$$\mathbf{S} = \begin{pmatrix} S_0 \\ S_1 \\ S_2 \\ S_3 \end{pmatrix} = \begin{pmatrix} E_x E_x^* + E_y E_y^* \\ E_x E_x^* - E_y E_y^* \\ E_x E_y^* + E_y E_x^* \\ i(E_x E_y^* - E_y E_x^*) \end{pmatrix} \tag{1}$$

5. Numerical and experimental results for a point-scatterer

An important practical issue in the measurement of the exit pupil polarization state distributions of the light scattered by the gold nano-sphere is to position the nano-sphere in the focal region of the high-NA objective. The auxiliary system shown in Fig. 2, formed by laser ALS (Spectra Physics He-Ne 196-1, λ = 633nm), lenses L2-L3 and L6, mirror M6 and camera CCD5, was implemented for this purpose. Laser ALS impinges upon the specimen from one side of the slide with the nano-spheres, rather than from the top or the bottom. This illumination configuration is equivalent to darkfield illumination in the sense that the light collected by the objective corresponds to purely scattered light with no light coming from a specular reflection or a transmission, see Fig. 6(a). Mirror M6 is in a flip-in mount such that when the mount is in the upright position the light collected by the high NA objective is deviated towards L6, which then forms an image of the specimen in camera CCD5. When the flip-in mount is lying down, the light follows its usual path in the vectorial polarimeter to form an image of the exit pupil in cameras CCD1-CCD4.

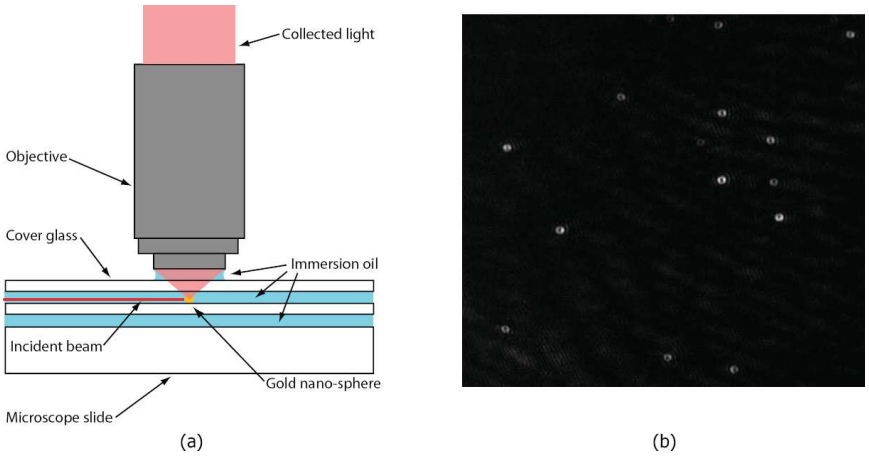

Fig. 6. (a) Diagram showing the preparation of the specimen and positioning with the auxiliary system; the specimen is being illuminated by the auxiliary laser, ALS. (b) Corresponding image of the nano-spheres as obtained by CCD5 with the flip-in mount mirror in the upright position.

Before presenting the results obtained for the gold nano-sphere, is convenient to describe briefly the preparation of the specimen. A drop of 80nm gold nano-spheres solution was put over a clean cover glass and spun around to spread the nano-spheres across its surface. The cover glass was then placed over a microscope slide with a drop of immersion oil between them to stick them together with an index matching medium. Next, an immersion oil drop

#124017 - $15.00 USD Received 9 Feb 2010; revised 27 Feb 2010; accepted 28 Feb 2010; published 3 Mar 2010

was put over the cover glass with the gold nano-spheres, and it was covered with a clean cover glass. The prepared specimen was then placed on a piezo nano-stage (PiezoSystems Jena, Tritor100SG) and positioned under the microscope objective for observation. Figures 6(a) and 6(b) are a diagram of the specimen prepared for positioning with the auxiliary darkfield system and the corresponding image obtained with CCD5, respectively. In this configuration, the nano-spheres act as point-like sources, and CCD5 shows the PSF of the auxiliary positioning system.

Although the image of the specimen in CCD5 was useful to find a gold nano-sphere and position it within the focal region of the high-NA objective, a fine adjustment was necessary to guarantee that the nano-sphere was on the optical axis. This adjustment was done by maximizing the irradiance distribution in the image of the exit pupil in one of the cameras of the system.

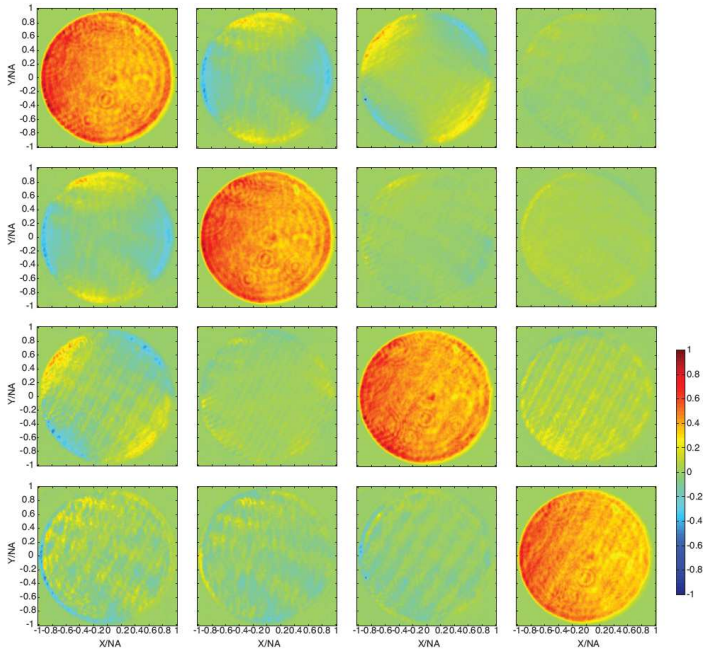

Fig. 7. Experimental Mueller matrix of the *on axis* 80nm gold nano-sphere measured with our system.

Our system measures complete scattering-angle-resolved Mueller matrices. Figure 7 shows the Mueller matrix distribution measured with our system for an *on axis* 80nm gold nano-sphere. The result shown here is the average of 5 frames on each CCD, for each incident polarization state, but no other digital smoothening filtering or post processing was applied. Each exposure was approximately 2s duration. The current limitations in our system's speed originate in the specifications of the equipment currently used. The measuring method itself is not limited to static specimens. In an application with particles in motion, for instance, much faster CCDs can be employed in combination with high-speed hardware data processing to adapt the system to the requirements of the application. A large amount of polarization information is contained in this experimental result. However, in the following subsections, to simplify the presentation of the results, we limit our discussion to Stokes parameters distributions that can be extracted from these experimental Mueller matrices. Thus, we present the Stokes parameters distribution in the exit pupil of the collector lens for three different positions of a gold nano-sphere in the focal plane along the *x*-axis (see Fig. 8): *on axis*, + λ/3, and –λ/3. The length of the *off axis* displacements was chosen arbitrarily with the only condition of it being a sub-resolution distance. The shortest measurable displacement of the gold nano-sphere is currently being explored in our laboratory. We show results for two

#124017 - $15.00 USD Received 9 Feb 2010; revised 27 Feb 2010; accepted 28 Feb 2010; published 3 Mar 2010

homogeneous incident polarization states before focusing, namely: linear horizontal and left-circular.

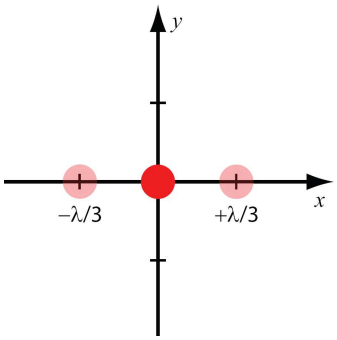

Fig. 8. Diagram of the focal plane with marks at the three positions of the point-scatterer (gold nano-sphere) analyzed. The origin of the *xy* coordinate system corresponds to the *on axis* position. The *z*-axis (not shown) is the optical axis of our system.

5.1 Incident light linearly polarized

Figure 9(a) shows the experimental results obtained for the *on axis* gold nano-sphere with incident light horizontally polarized [36]. Figure 9(b) shows the corresponding numerical results for a point-scatterer under the same oil immersion and illumination conditions. These results are normalized with respect to the maximum S_{0x}. The basic structure of the experimental polarization state distribution is clear and in agreement with the results presented in Fig. 9(b), despite the noise in the experimental results, and the slight horizontal asymmetry of S_{0x} and S_{1x}, not present in the numerical results. The noise in the experimental results is consistent with the noise in the Mueller matrix of the calibration samples. For instance, the distribution of S_{3x} is the same as the spurious interference fringes discussed in section 3. Thus, this distribution does not contain information about the specimen under observation but about the current imperfections of our optical system.

Figures 10(a) and 11(a) show the experimentally determined Stokes parameters distribution in the exit pupil for an *off axis* point-scatterer located in the focal plane at $x = -\lambda/3$ and $x = +\lambda/3$, respectively, with incident light linearly polarized in the horizontal direction. The corresponding numerical results are shown in Figs. 10(b) and 11(b). The previous figures show that, despite noise in the measurements, the general form of the measured distributions is the same as in the numerical calculations. Furthermore, the mirror symmetry, along the horizontal direction, predicted for S_{3x} between the $x = -\lambda/3$ and $x = +\lambda/3$ positions of the scatterer, is clearly present in the experimental results. Our results show that it is possible to determine if the sub-resolution scatterer has undergone a sub-resolution displacement, as well as the direction of the sub-resolution displacement, by analyzing the polarization state distribution in the exit pupil of the high-NA collector lens.

#124017 - $15.00 USD Received 9 Feb 2010; revised 27 Feb 2010; accepted 28 Feb 2010; published 3 Mar 2010

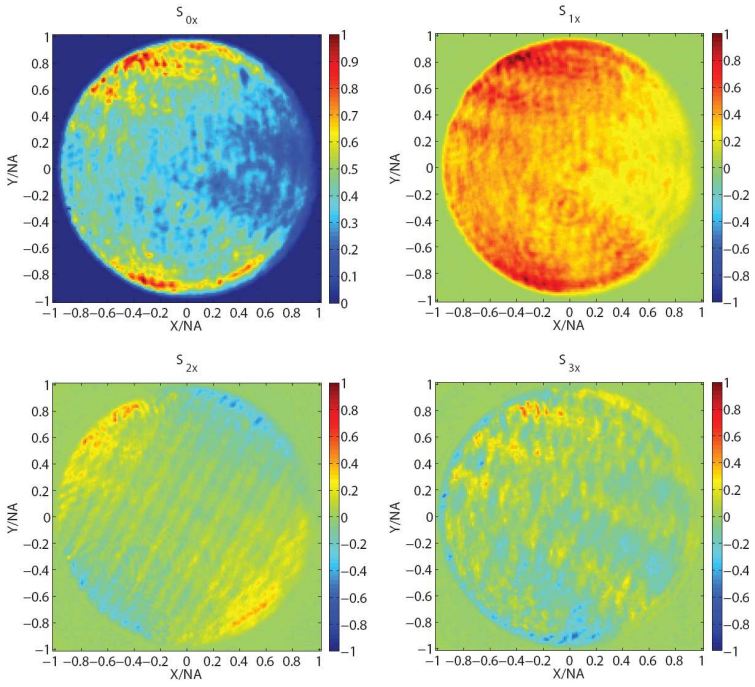

(a)

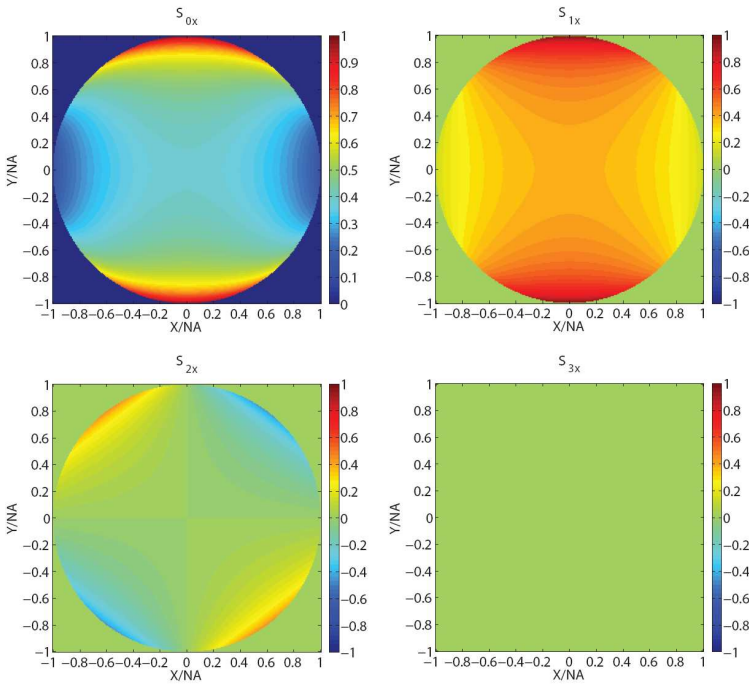

(b)

Fig. 9. (a) Experimentally obtained Stokes parameters distribution in the exit pupil of the collector lens for an *on axis* gold nano-sphere with incident light linearly polarized in the horizontal direction. (b) Corresponding numerical results for a point-scatterer. The Stokes parameters are normalized with respect to the maximum S_{0x}.

#124017 - $15.00 USD Received 9 Feb 2010; revised 27 Feb 2010; accepted 28 Feb 2010; published 3 Mar 2010

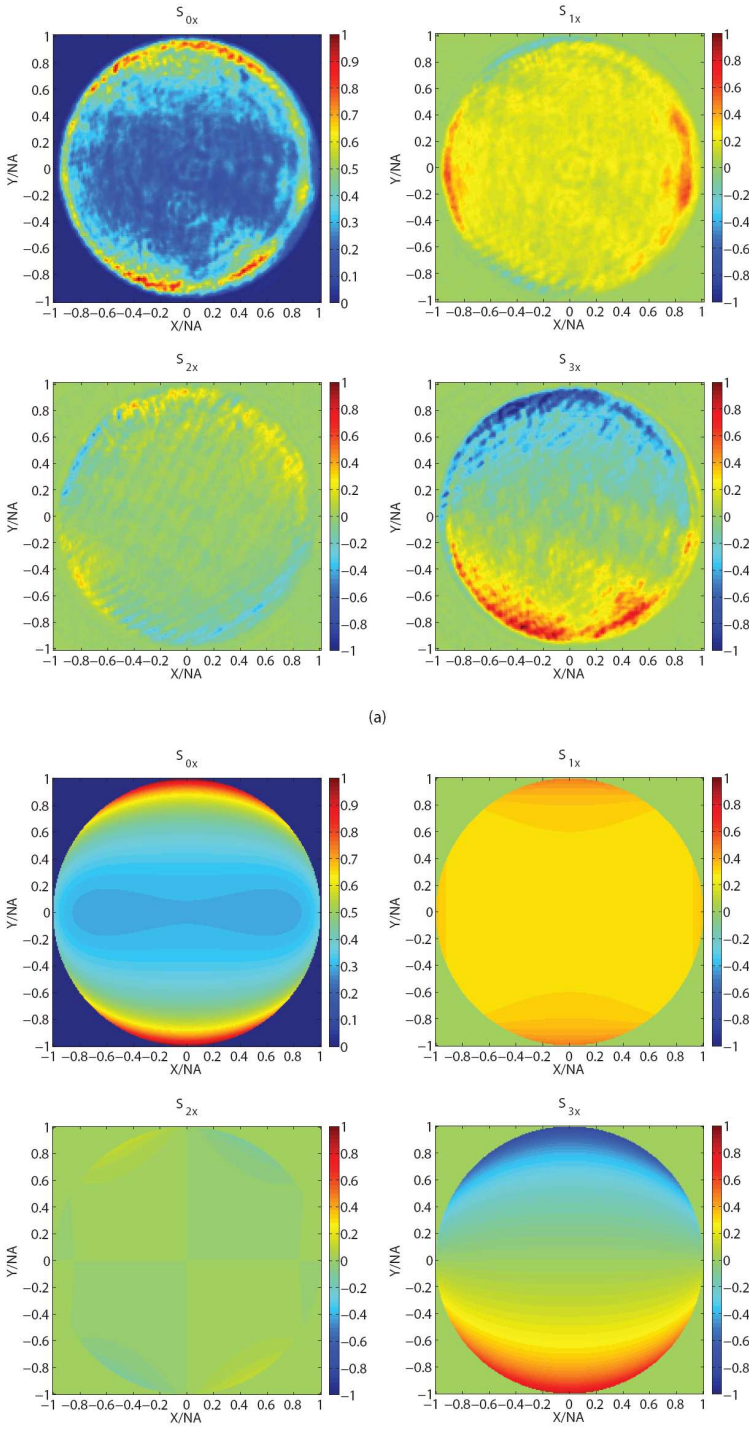

Fig. 10. (a) Experimentally obtained Stokes parameters in the exit pupil of the collector lens for a gold nano-sphere in the focal plane at $x = -\lambda/3$ with incident light linearly polarized in the horizontal direction. (b) Corresponding numerical results for a point-scatterer. The Stokes parameters are normalized with respect to the maximum S_{0x}.

#124017 - $15.00 USD Received 9 Feb 2010; revised 27 Feb 2010; accepted 28 Feb 2010; published 3 Mar 2010

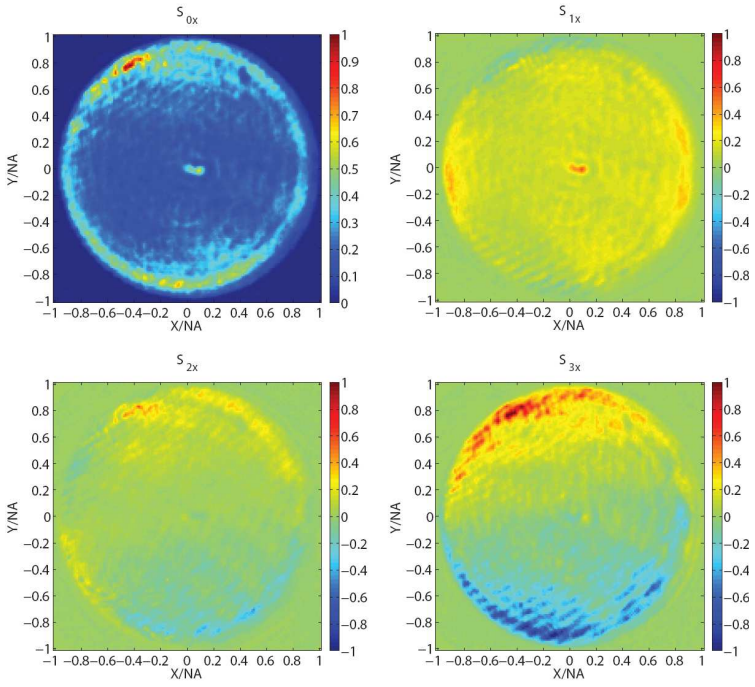

(a)

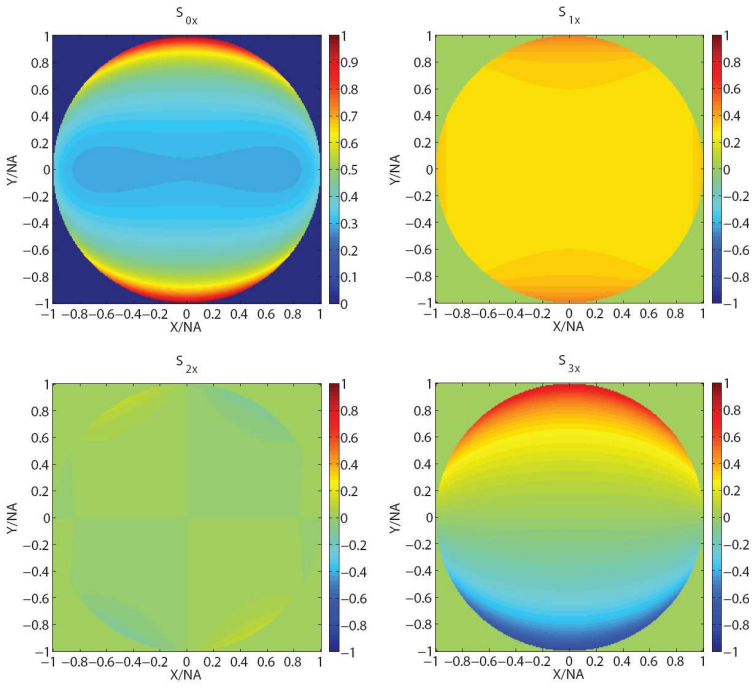

(b)

Fig. 11. (a) Experimentally obtained Stokes parameters in the exit pupil of the collector lens for a gold nano-sphere in the focal plane at $x = +\lambda/3$ with incident light linearly polarized in the horizontal direction. (b) Corresponding numerical results for a point-scatterer. The Stokes parameters are normalized with respect to the maximum S_{0x}.

#124017 - $15.00 USD Received 9 Feb 2010; revised 27 Feb 2010; accepted 28 Feb 2010; published 3 Mar 2010

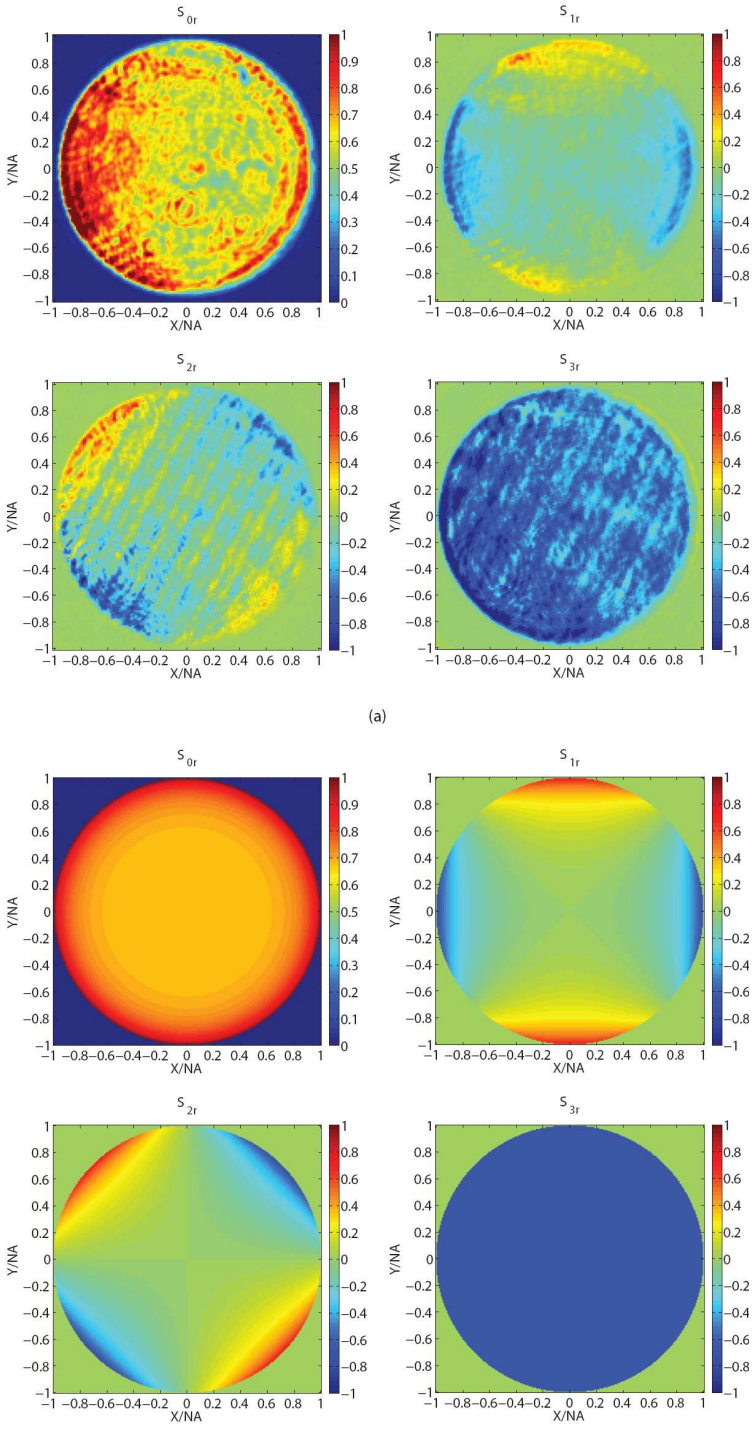

Fig. 12. (a) Experimentally obtained Stokes parameters distribution in the exit pupil of the collector lens for an *on axis* gold nano-sphere with incident light circularly polarized to the left. (b) Corresponding numerical results for a point-scatterer. The Stokes parameters are normalized with respect to the maximum S_{0r}.

#124017 - $15.00 USD Received 9 Feb 2010; revised 27 Feb 2010; accepted 28 Feb 2010; published 3 Mar 2010

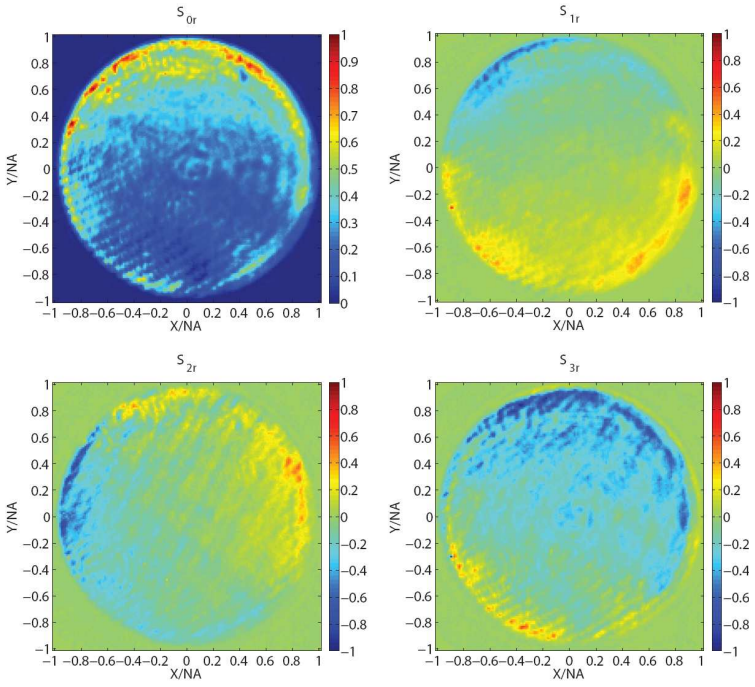

(a)

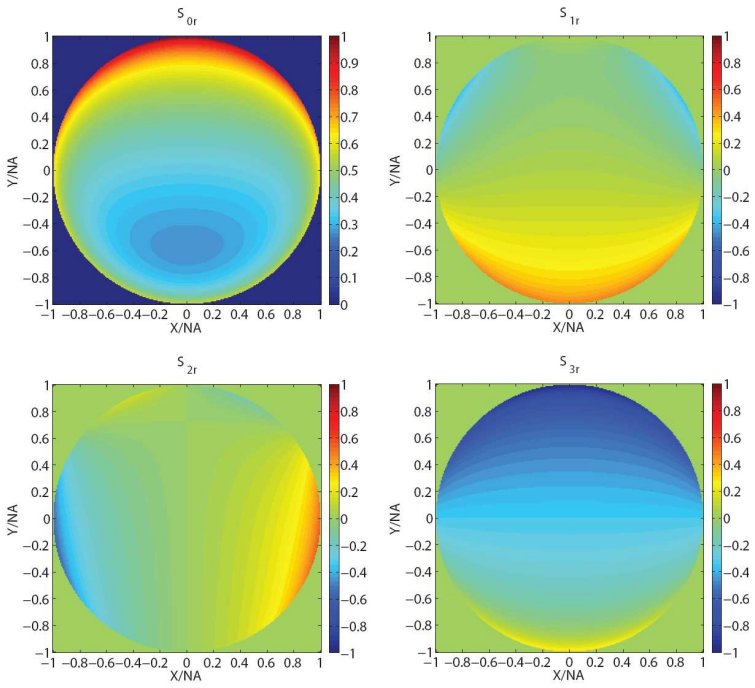

(b)

Fig. 13. (a) Experimentally obtained Stokes parameters in the exit pupil of the collector lens for a gold nano-sphere in the focal plane at $x = -\lambda/3$ with incident light circularly polarized to the left. (b) Corresponding numerical results for a point-scatterer. The Stokes parameters are normalized with respect to the maximum S_{0r}.

#124017 - $15.00 USD Received 9 Feb 2010; revised 27 Feb 2010; accepted 28 Feb 2010; published 3 Mar 2010

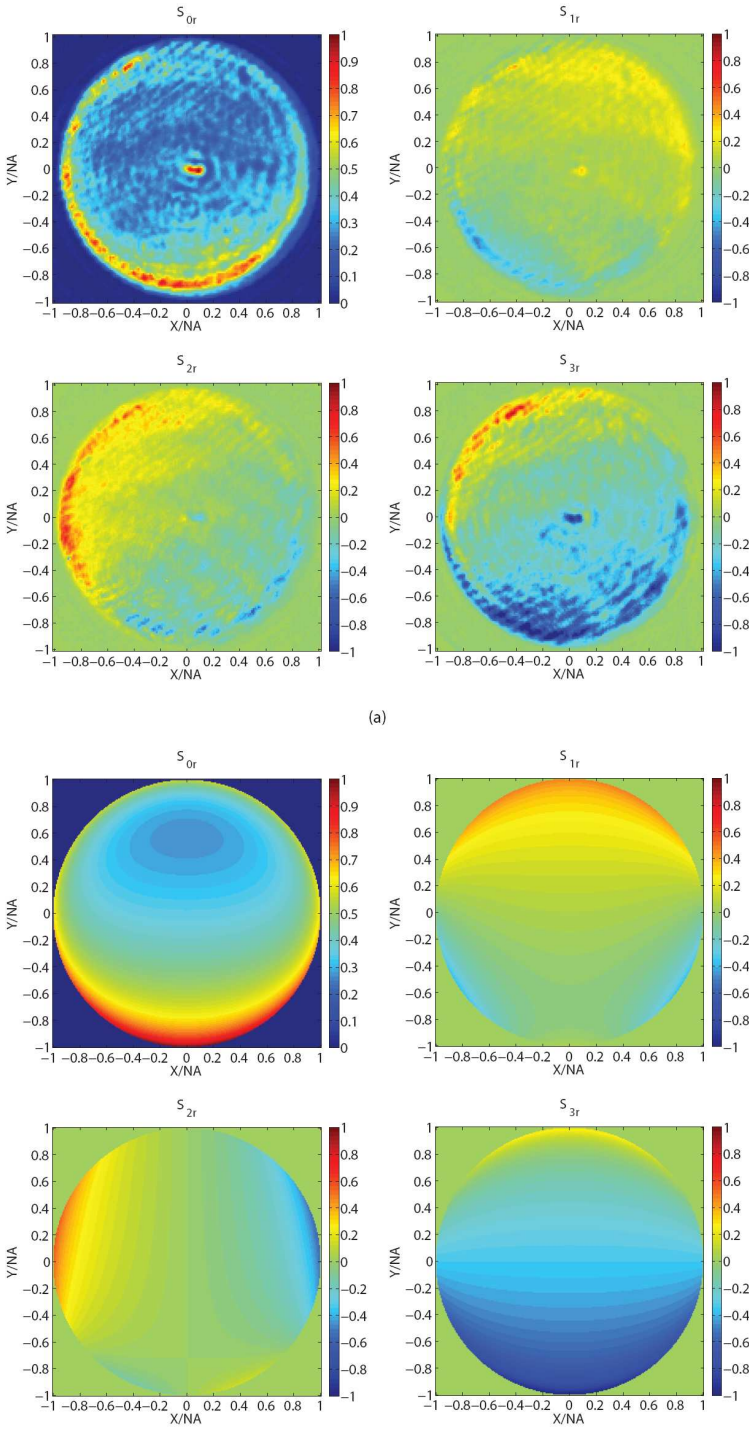

Fig. 14. (a) Experimentally obtained Stokes parameters in the exit pupil of the collector lens for a gold nano-sphere in the focal plane at $x = +\lambda/3$ with incident light circularly polarized to the left. (b) Corresponding numerical results for a point-scatterer. The Stokes parameters are normalized with respect to the maximum S_{0r}.

#124017 - $15.00 USD Received 9 Feb 2010; revised 27 Feb 2010; accepted 28 Feb 2010; published 3 Mar 2010

5.2 Incident light circularly polarized

Figure 12(a) shows the experimental results obtained for the *on axis* gold nano-sphere for incident light circularly polarized to the left. The corresponding numerical results are shown in Fig. 12(b). Once more, the basic structure of the Stokes parameters distribution in the exit pupil of the collector lens is apparent and in agreement with the numerical results. The noise in Fig. 12(a) is also consistent with the expected residual polarization artifacts that remain after the calibration.

As shown in the results presented in subsection 5.1, the sensitivity to the direction of the sub-resolution displacement of the point-scatterer is limited to S_{3x} in the case of incident light linearly polarized. The other three Stokes parameters exhibit the same distribution independently of the direction of the displacement. However, as will be explained below, the sensitivity of our system depends on the electric field distribution in the focal region. The use of incident light circularly polarized allows us to achieve the high sensitivity in any of the four Stokes parameters. Figures 13(a) and 14(a) show the experimental results obtained for circularly polarized light. The corresponding numerical results are shown in Figs. 13(b) and 14(b). The agreement between numerical and experimental results is clear, in most of the Stokes parameters. The element with the worst agreement with its numerical counterpart, especially in the results for the gold nano-sphere at $x = -\lambda/3$, is S_{2r}. Thus, due to the relatively high noise level in the experimentally determined S_{2r}, no conclusive remarks, based on this element, can be made concerning the displacement of the gold nano-sphere. Nevertheless, as can be seen in Figs. 13(a) and 14(a), the direction of the sub-resolution displacement of the gold nano-sphere is encoded in the other three Stokes parameters, as predicted by the numerical calculations.

6. Discussion

We presented an instrument that measures the scattering-angle-resolved Mueller matrix across the exit pupil of a high-NA collector lens as a means to analyze the three-dimensional field resulting from the interaction of a three-dimensional focused field and a sub-resolution specimen. The instrument is a scattering-angle-resolved Mueller matrix polarimeter that allows for high sensitivity to sub-resolution displacements of a sub-resolution scatterer. First experimental evidence showing the high sensitivity of the system, together with its corresponding numerical calculations, has been provided. Our experimental results agree with the numerical calculations performed to assess the feasibility of our system. The experimental distributions of the Stokes parameters on the back focal plane of a high-NA system correspond to our numerical predictions, that use established methods. As in any experimental system, our measurements contain noise and errors. The accuracy of our measurements was verified by measuring known samples in double-pass, and the results were always within 3% of the largest Mueller matrix coefficient (transmittance) of the mean value of the pupil distribution. Light scattered by an 80 nm gold nano-sphere was measured and calibrated successfully.

Our experimental results show that the residual polarization artifacts are caused by the interference fringes discussed in section 3. We showed that our assumption of no polarization artifacts introduced by the objective, at a first approximation, is appropriate within the limitations of our experimental setup. Modifications to reduce the error in the measurements may be required to improve the reliability of the system when applied to small scatterers. One possibility is to replace the current simultaneous PSA for a single CCD system with sequential polarization analyzers. The low contrast interference fringes in the pupil images would become common to all polarization signals, provided the sample does not move between measurements. In this way, we could apply a post-processing filter to reduce the effect of these fringes. We are aware that a thorough error analysis of the system we present is required, but this falls beyond the scope of this work. We have used robust calibration methods and are confident that our results are reliable, at least to a first approximation. This was verified by our numerical results.

#124017 - $15.00 USD Received 9 Feb 2010; revised 27 Feb 2010; accepted 28 Feb 2010; published 3 Mar 2010

We have analyzed numerical values of the components of the electric field in the focal region of the high-NA focusing lens. Our preliminary study revealed that, for incident light linearly polarized in the horizontal direction, the *y* component of the electric field is zero along the *x*-axis, whereas the *x* component has the same value at both *off axis* positions of the scatterer. The value of the *z* component at $x = -\lambda/3$, on the other hand, is the negative of its value at $x = +\lambda/3$. Similarly, for the case of incident light circularly polarized, the *x* and *y* components of the electric field are equal, and different from zero, for both *off axis* positions. For circularly polarized light the *z* component at $x = -\lambda/3$ is also the negative of its value at $x = +\lambda/3$. It seems that the asymmetry in the focused field distribution, associated to the *z* component, is the key to differentiate between the two *off axis* positions.

In its current state, our method does not provide a quantitative measure of the magnitude of the displacement undergone by the sub-resolution scatterer, although it provides information on the direction of the displacement. The definition of a suitable metric, with an appropriate threshold, based on the statistical properties of the polarization distribution across the exit pupil of the collector lens is work in progress and we intend to report it in a future stage.

Acknowledgments

We are grateful to Klas Lindfors and Prof. Ari T. Friberg, from the Helsinki University of Technology, for the preparation of the gold nano-spheres used as specimen in this research. This project was funded by Science Foundation Ireland through grants 01/PI.2/B039C and 07/IN.1/I906, and Shimadzu Corporation, Japan. Oscar G. Rodríguez-Herrera is grateful to the National Council for Science and Technology (CONACYT, Mexico) for the PhD scholarship 177627.

#124017 - $15.00 USD Received 9 Feb 2010; revised 27 Feb 2010; accepted 28 Feb 2010; published 3 Mar 2010